Two-Phase Flow Properties and Free-Surface Deformations in Hydraulic Jumps

Hang Wang[1], Hubert Chanson[1]

[1] *The University of Queensland, School of Civil Engineering, Brisbane, Australia*

Keywords: hydraulic jump, two-phase flow, free-surface fluctuations, turbulence, physical modelling

Abstract

In an open channel, a hydraulic jump is a sudden transition from a high-velocity to slower, fluvial flow motion. The impinging flow forms a turbulent roller with a highly fluctuating free-surface, while a large amount of air bubbles is entrapped at the jump toe. The present work presents some physical investigations of hydraulic jumps based upon a wide range of inflow Froude numbers ($3.8 < Fr_1 < 10.0$) and Reynolds numbers ($2.1 \times 10^4 < Re < 1.6 \times 10^5$). Both the Froude and Reynolds similarities were tested independently. Free-surface deformations were measured non-intrusively with fast-response sensors. The shape of free-surface profile was clearly defined, and maximum fluctuations were observed in the first half of the roller. Characteristic fluctuation frequencies were seen between 0.5 and 3.5 Hz, including both dominant and secondary frequencies. The free-surface fluctuation data were analysed and linked to the longitudinal roller movement, showing some simultaneous motions of the roller surface in both horizontal and vertical directions. Wave propagation at the roller free-surface presented some celerity close to the advection speed of large vortices in the roller shear region. A phase-detection probe was used to measure the two-phase flow properties, including void fraction and bubble count rate. The interaction between the instantaneous two-phase flow properties and free-surface deformations was documented by some simultaneous surface location and sub-millimetric air-water flow measurements. Different features were exhibited depending upon the phase-detection location in different regions of the roller.

Introduction

A hydraulic jump forms in an open channel when a high-velocity inflow impinges into a slower flow region. The downstream water level is significantly higher than the upstream water level and a turbulent roller is generated downstream of the impingement point, with substantial air entrainment into the roller, significant fluctuations at the free-surface as well as change of longitudinal roller positions (Fig. 1). The free-surface deformations are related to the two-phase flow properties and turbulence development in the roller, although these interactions are not fully understood because of the large number of relevant parameters and complicated flow regimes. Early investigations in terms of free-surface elevations included Madsen (1981), Kucukali & Chanson (2008), Mouaze et al. (2005), Murzyn & Chanson (2009a), and Chachereau & Chanson (2011). A few studies used some imaging techniques to characterise the free-surface properties (Mossa & Tolve 1998, Leandro et al. 2012). For the physical modelling of hydraulic jumps, both inflow Froude number Fr_1 and Reynolds number Re are relevant dimensionless numbers (Chanson 2007). But a dynamic similitude cannot be satisfied by achieving identical Froude and Reynolds numbers using the same fluids in model and prototype (Liggett 1994, Chanson 2009).

In the present study, the effects of inflow Froude number and Reynolds number on the fluctuating natures of hydraulic jump were investigated separately. Some characteristic frequencies of the fluctuating motions were documented, and simultaneous free-surface deformations in both horizontal and vertical directions were recorded. Further information in the interaction between air entrainment and turbulent roller motions was provided by simultaneous air-water flow and free-surface fluctuation measurements.

Nomenclature

C	time averaged void fraction
c	instantaneous void fraction
d	water depth (m)
F	1. characteristic frequency (Hz)
	2. air bubble count rate (Hz)
Fr_1	inflow Froude number $Fr = V_1/(g \times d_1)^{1/2}$
g	gravity acceleration (m s^{-2})
h	upstream sluice gate opening (m)
Q	flow rate (m^{3}s^{-1})
R	normalised correlation coefficient
Re	Reynolds number $Re = \rho \times V_1 \times d_1/\mu$
t	time (s)
U	wave propagation celerity at free-surface (ms^{-1})
V	velocity (ms^{-1})
W	channel width (m); herein W = 0.5 m
x	longitudinal position (m)
y	vertical position (m)
z	transverse location (m)

Greek letters

μ	dynamic viscosity (Pa s)
η	water elevation (m)
ρ	water density (kg m^{-3})

τ time lag (s)
Subscripts
1   upstream flow conditions
2   downstream flow conditions
dom   dominant frequency
ej   ejection of large scale vortices in shear layer
fs   free-surface
max   maximum
sec   secondary frequency
toe   jump toe

(A) General view showing the acoustic displacement meters upstream of and above the roller; flow direction from right to left – Flow conditions: $Q = 0.0368$ m^3/s, $d_1 = 0.0277$ m, $x_1 = 1.083$ m, $Fr_1 = 5.1$, $Re = 7.4 \times 10^4$.
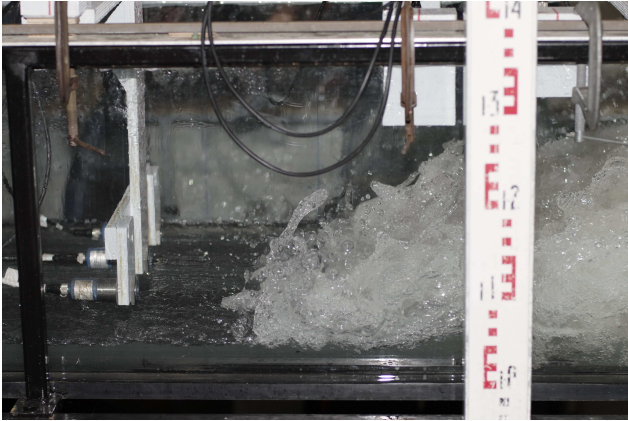
(B) Side view of a hydraulic jump with flow direction from left to right - Note the acoustic displacement meters (left) upstream of and above the roller- Flow conditions: $Q = 0.0552$ m^3/s, $d_1 = 0.0363$ m, $x_1 = 1.417$ m, $Fr_1 = 5.1$, $Re = 1.1 \times 10^5$.
Figure 1: Physical modelling of hydraulic jumps in the 0.5 m wide channel.

Experimental Instrumentation and Signal Processing

The experiments were performed in a 3.2 m long and 0.5 m wide horizontal rectangular channel. The channel bed was made of smooth PVC and the sidewalls were 3.2 m long 0.41 m high glass panels. The upstream and downstream flow conditions were controlled respectively by an undershoot sluice mounted in an upstream head tank and an overshoot sluice at the end of channel. Figure 2 sketches the experimental setup, denoting the sluice opening h, conjugate depths d_1 and d_2, longitudinal jump toe position x_1 and length of jump roller L_r. Further relevant parameters are also

defined. The water discharge was measured with Venturi meters and the clear-water depth was recorded with a pointer gauge.

Up to 15 acoustic displacement meters (Microsonic™ Mic+25/IU/TC & Mic+35/IU/TC) were used to record simultaneously the instantaneous free-surface positions at various locations. Figure 1A shows all 15 sensors in position around the roller, while three displacement meters are seen in Figure 1B (Left). The displacement meters detected the water surface by emitting acoustic beams and capturing the reflected ones. The distance between the sensor head and water surface was derived from the travel time of the acoustic beam. The sensors had a response time typically less than 50 ms, and each sensor was sampled continuously at 50 Hz (unless otherwise stated). The voltage outputs contained some erroneous signals caused by missed acoustic beams or beams reflected by splashing droplets. The erroneous samples were removed using some simple threshold techniques. The processed signals were converted into water depth data based upon calibration curves obtained on-site.

The air-water flow properties were measured with an intrusive phase-detection conductivity probe that discriminated between air and water phases by their different electrical conductivities. The phase-detection probe had two needle sensors with inner diameter $\emptyset = 0.25$ mm. The probe was excited by an electronic system (model Ref. UQ82.518) designed with a response time less than 10 μs. The probe was typically sampled at 20 kHz for 45 s (Chanson 2007). However, for simultaneous sampling with the acoustic displacement meters, the sampling rate was set at 5 kHz to match the relative slow response of displacement meters. In all the cases, the voltage signals were processed using a signal threshold technique, the threshold being set at 50% of the air-water range.
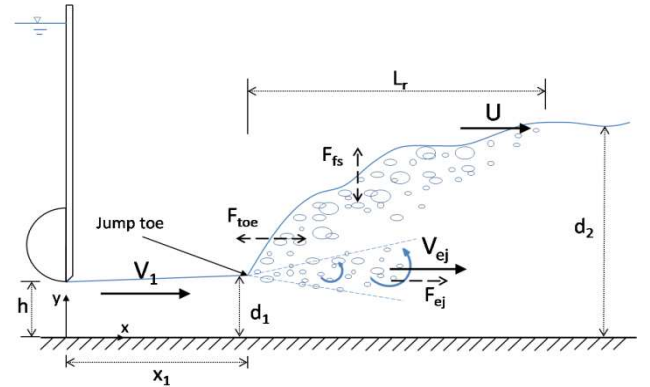

Figure 2: Sketch of the experimental hydraulic jump.
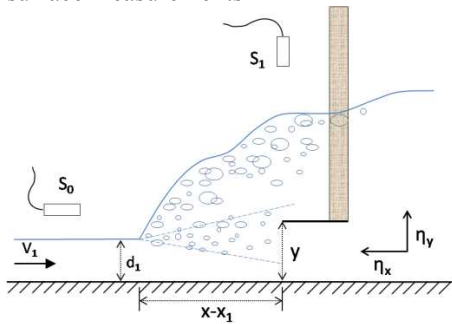
Experimental flow conditions
Figure 1 shows two photographs of the acoustic displacement meter arrangement for the free-surface measurements. A cross-sectional sketch is shown in Figure 3A. On the channel centreline, a displacement meter was located horizontally above the inflow surface, with the sensor head facing the jump front from upstream, while several displacement meters were placed vertically above the roller. Two series of experiments were conducted with this setup based upon different similitude criteria, i.e., a series was conducted with a fixed gate opening h and various inflow Froude numbers ($3.8 < Fr_1 < 10.0$), while the

second series was performed with an identical Froude number (Fr_1 = 5.1) but different gate openings, hence a range of Reynolds numbers ($2.1 \times 10^4 < Re < 1.6 \times 10^5$) (Table 1).

The experimental setup for simultaneous measurements of free-surface motions and air entrapment is shown in Figure 3B. At a given longitudinal position x-x_1, the vertical displacement meter was aligned over the phase-detection probe tip. The height of the horizontal displacement meter was fixed when the phase-detection probe was located at different elevations y in the roller. The experiments were performed at two longitudinal positions, namely $(x-x_1)/d_1$ = 4 & 8, with three Reynolds numbers for the same Froude number Fr_1 = 5.1 (Table 1). All flow conditions are reported in Table 1 where the corresponding instrumentation is noted: ADM = acoustic displacement meters, and PDP = phase-detection probe.
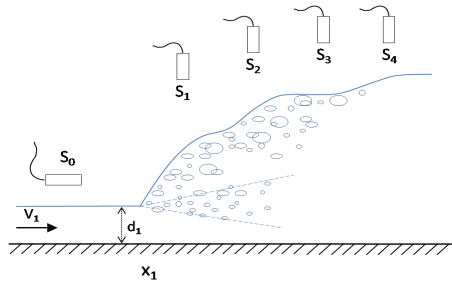
(A) Free-surface measurements

(B) Simultaneous free-surface and air-water flow measurements
Figure 3: Sketch of experimental setups – (A, top) Free-surface measurements; (B, bottom) Simultaneous free-surface and air-water flow measurements.

Table 1: Experimental flow conditions and instrumentation.

Q (m^3/s)	h (m)	x_1 (m)	d_1 (m)	Fr_1	Re	Comment
0.0160	0.012	0.5	0.012	5.1	2.1×10^4	ADM
0.0179	0.020	0.83	0.0206	3.8	3.5×10^4	ADM
0.0239			0.0209	5.1	4.8×10^4	ADM+PDP
0.0347			0.0206	7.5	6.8×10^4	ADM
0.0397			0.0208	8.5	8.0×10^4	ADM
0.0473			0.021	10.0	9.5×10^4	ADM
0.0368	0.026	1.083	0.0277	5.1	7.4×10^4	ADM
0.0352	0.030	1.25	0.0326	3.8	7.0×10^4	ADM+PDP
0.0461			0.0322	5.1	9.2×10^4	ADM
0.0709			0.033	7.5	1.41×10^5	ADM
0.0552	0.034	1.417	0.0363	5.1	1.10×10^5	ADM
0.0689	0.040	1.667	0.042	5.1	1.37×10^5	ADM+PDP
0.0815	0.045	1.875	0.047	5.1	1.63×10^5	ADM
0.0820	0.054	1.25	0.057	3.8	1.62×10^5	ADM

Notation: Q: flow rate; h: sluice opening; x_1: longitudinal jump toe position; d_1: inflow water depth; Fr_1: inflow Froude number; Re: Reynolds number; ADM: acoustic displacement meter; PDP: phase-detection probe.
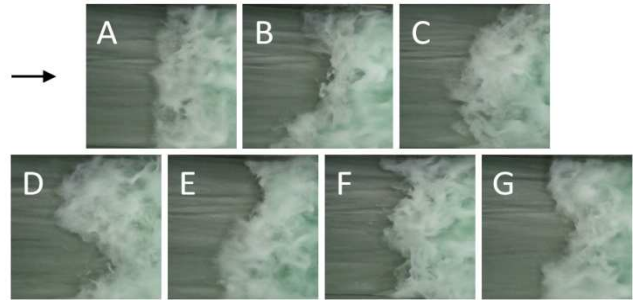

Figure 4: Instantaneous transverse impingement perimeter profiles – Flow direction from left to right.

Results and Discussion

Basic free-surface profiles

Traditionally, a stationary hydraulic jump is analysed as a two-dimensional flow pattern, neglecting any transverse flow feature except very close to the channel sidewalls. In the present study, however, the instantaneous transverse impingement perimeter exhibited some clearly marked fluctuating profiles, though the average was nearly a straight line. Several typical transverse profiles are presented in Figure 4, as viewed in elevation. Some transverse wave patterns were seen with the ratio of wave length to channel width l_w/W between 2/3 and 2 (Zhang et al. 2013). The transverse fluctuations increased with increasing Froude number, and the time-averaged fluctuation amplitude was nearly independent of the transverse location z for $-0.6 < z/(W/2) < 0.6$, with $z = 0$ on the channel centreline.

The time-averaged water elevations η on the channel centreline showed some profiles close to the visually observed free-surface shape. The dimensionless relative elevation $(\eta-d_1)/(d_2-d_1)$ presented some self-similarity within the length of jump roller for a range of flow conditions, with d_1 and d_2 being the upstream and downstream flow depths (Fig. 2). The results are shown in a self-similar presentation in Figure 5A together with the correlation function:

$$\frac{\eta - d_1}{d_2 - d_1} = \left(\frac{x-x_1}{L_r}\right)^{0.727} \tag{1}$$

where the roller length L_r was defined as the distance over which the mean free-surface level increased monotonically (Murzyn & Chanson 2009b). Some results of Chanson (2011) are also included in Figure 5A for comparison.

Some typical fluctuations of free-surface elevations are shown in terms of the dimensionless standard deviations of the instantaneous water elevation data η'/d_1 in Figure 5B. The data indicated that the maximum fluctuations were observed in the first half roller. The fluctuation level increased with increasing Froude number. A quasi-linear relationship was suggested between the maximum deviation η'_{max}/d_1 and the inflow Froude number. Altogether the data were qualitatively and quantitatively close to the earlier findings of Mouaze et al. (2005) and Murzyn & Chanson (2009). Note that the value of free-surface elevation standard deviation could be affected by the thresholds used in the erroneous data removal during the displacement meter

signal processing.
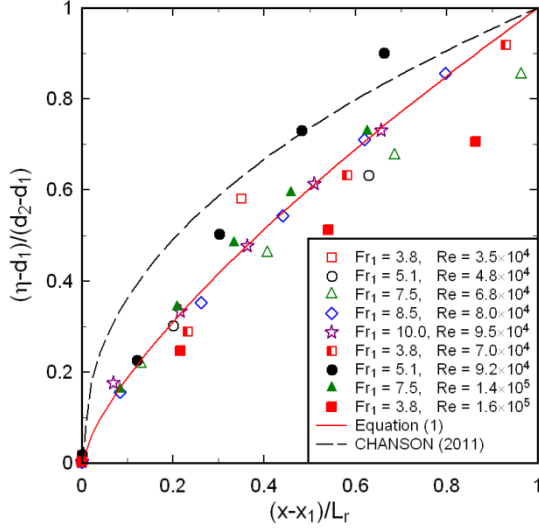
(A) Time-averaged relative free-surface elevations
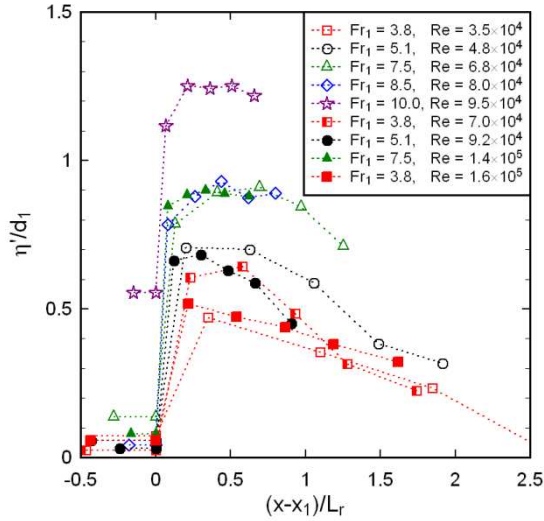
(B) Standard deviation of free-surface fluctuations
Figure 5: Free-surface profile and fluctuations – (A, top) Time-averaged relative free-surface elevations; (B, bottom) Standard deviation of free-surface fluctuations.

Characteristic frequencies of the roller surface motion
Spectral analyses of the displacement meter signals provided some information on the characteristic frequencies of the free-surface fluctuations. All the free-surface data were analysed and the results showed consistently a dominant frequency commonly shown by a marked peak in the power spectrum density function, as well as one or more secondary frequencies highlighted by some lesser peaks in energy density. Sometimes a small range of frequencies were observed rather than a unique value. The dominant and secondary characteristic frequencies of free-surface fluctuations were documented, and denoted $F_{fs,dom}$ and $F_{fs,sec}$ respectively.

The characteristic frequencies were observed within similar ranges at different longitudinal positions on the channel centreline. For a broad range of Froude and Reynolds numbers ($3.8 < Fr_1 < 10.0$ and $3.5 \times 10^4 < Re < 1.6 \times 10^5$), the dominant free-surface fluctuation frequencies were typically between 1.2 and 3.5 Hz, and the secondary frequencies were between 0.5 and 1.2 Hz (Table 2). The dimensionless

frequencies $(F_{fs} \times d_1)/V_1$ showed some exponential decay trend with increasing inflow Froude number, whereas no obvious effect of the Reynolds number was seen. Figure 6 presents the dimensionless dominant and secondary free-surface fluctuation frequencies as functions of the Froude number. In Figure 6, the data are compared with the following correlation functions:

$$\frac{F_{fs,dom} \times d_1}{V_1} = 0.163 \times \exp(-0.36 \times Fr_1) \quad (2a)$$

$$\frac{F_{fs,sec} \times d_1}{V_1} = 0.021 \times \exp(-0.19 \times Fr_1) \quad (2b)$$

The free-surface fluctuations were also measured by Chachereau & Chanson (2011) with a similar metrology for $Fr_1 < 5.1$. Their data were best correlated by

$$\frac{F_{fs} \times d_1}{V_1} = 0.143 \times \exp(-0.27 \times Fr_1) \quad (3)$$

Both Equation (2a) and (3) showed a similar trend for a wide range of Froude numbers (Fig. 6).

For the secondary frequencies, the present data were qualitatively and quantitatively comparable with some previous observations, namely the frequency of longitudinal jump toe oscillation F_{toe} and the frequency of downstream ejection of large scale vortices F_{ej} (Zhang et al. 2013). In the hydraulic jump, the jump toe oscillated longitudinally around its mean position x_1, while large vortices were successively formed and advected downstream in the roller shear layer. These two fluctuating motions are sketched in Figure 2 with dashed arrows, together with the free-surface fluctuation motion. Zhang et al. (2013) observed the oscillation frequency F_{toe} and vortices advection frequency F_{ej} by means of video cameras. Their data were best correlated to the inflow Froude number as

$$\frac{F_{toe} \times d_1}{V_1} = 0.054 \times \exp(-0.33 \times Fr_1) \quad (4)$$

$$\frac{F_{ej} \times d_1}{V_1} = 0.034 \times \exp(-0.26 \times Fr_1) \quad (5)$$

Equation (4) and (5) are plotted in Figure 6, comparing well with the secondary frequency data and Equation (2b).
It is believed that the oscillation of jump toe and the generation and advection of large scale vortices in the roller were related to each other (Long et al. 1990, Chanson 2010). The presence of the secondary free-surface fluctuation frequencies with similar distributions implied that the jump toe oscillation and vortices advection might also interact with the free-surface fluctuations.
The rapid shift of instantaneous longitudinal jump toe position about its mean position x_1, namely the jump toe oscillation, was recorded using horizontal acoustic displacement meters (e.g. sensor S_0 in Fig. 3A). These displacement meters detected the jump roller front moving back and forth together with the oscillating jump toe (Fig. 1B). The characteristic frequencies of the motion were derived based upon spectral analysis on the relative surface position data. Both dominant and secondary characteristic frequencies were observed, with the dominant frequency approximately between 0.5 and 1.3 Hz and secondary frequency between 0.8 and 2.6 Hz (Table 2). Figure 7 presents the dimensionless jump toe oscillation frequency data as function of the inflow Froude number. Some data were recorded with a constant Froude number ($Fr_1 = 5.1$) for different gate openings h, while other data were

collected with a fixed gate opening (h = 0.020 m) for a range of Froude numbers (Fr_1 = 3.8, 5.1, 7.5 & 8.5). Some visual observations by Zhang et al. (2013), Chanson (2005, 2010), Murzyn & Chanson (2009b) and Chachereau & Chanson (2011) are also plotted in Figure 7. The present data with identical Froude number showed a range of dimensionless frequencies, implying some form of scale effects related to the differences in Reynolds numbers. The dominant frequencies were close to the visual observations of jump toe oscillations, but for the data of Zhang et al. (2013) and Chachereau & Chanson (2011) at low Froude numbers (Fr_1 < 4.4). The difference might be linked with some difficulty to aim the displacement meter at the jump front close to the jump toe at small hydraulic jumps.
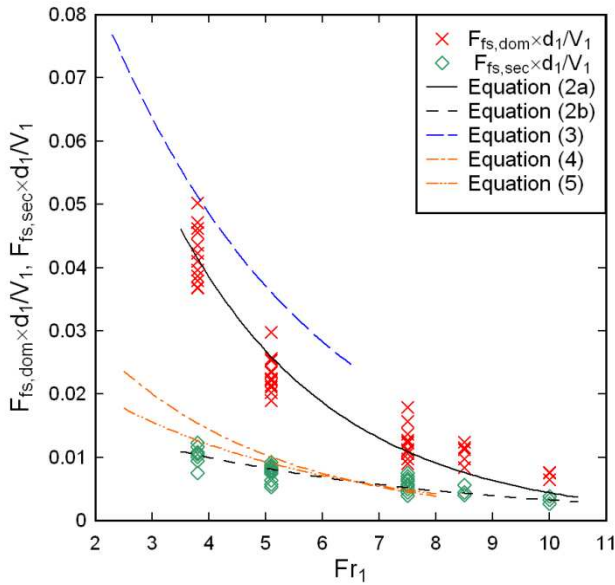

Figure 6: Dimensionless free-surface fluctuation frequencies as functions of inflow Froude number – Comparison with the experimental results of Chachereau & Chanson (2011) and Zhang et al. (2013).
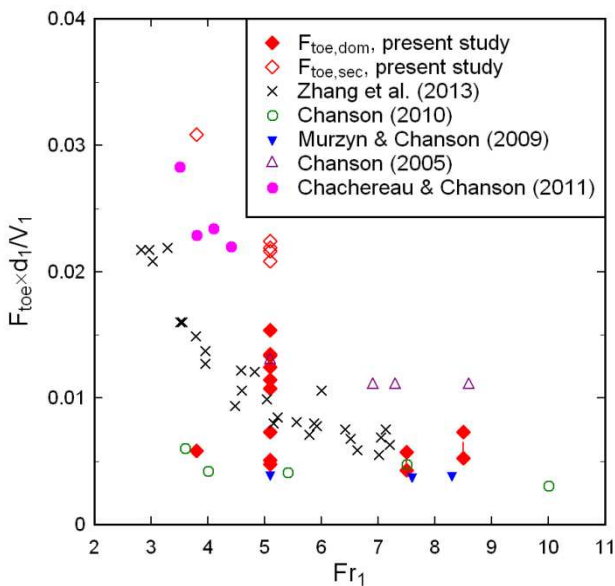

Figure 7: Dimensionless jump toe oscillation frequencies as functions of inflow Froude number – Comparison with experimental observations of Chanson (2005, 2010), Murzyn & Chanson (2009b), Chachereau & Chanson (2011)

and Zhang et al. (2013).

A comparison between the characteristic frequencies of jump toe oscillations in horizontal direction and free-surface fluctuations in vertical direction showed that the dominant jump toe oscillation frequencies $F_{toe,dom}$ had a similar range to the secondary free-surface fluctuation frequencies $F_{fs,sec}$, while the secondary jump toe oscillation frequencies $F_{toe,sec}$ were within a similar range corresponding to the dominant free-surface fluctuation frequencies $F_{fs,dom}$. Table 2 summarises the observations in term of frequency ranges. All data were measured with acoustic displacement meters on the channel centreline. The observations supported the suggestion that the horizontal jump toe oscillations and vertical free-surface fluctuations were related. They further implied that these two processes had different behaviour because they had different primary characteristic frequencies. It is thought that the interaction between the two motions was reflected by some secondary frequencies.

Table 2: Characteristic frequency ranges of free-surface fluctuations and jump toe oscillations (acoustic displacement meter data).

|	F_{fs} (Hz)	F_{toe} (Hz)
Dominant	1.2 / 3.5	0.5 / 1.3
Secondary	0.5 / 1.2	0.8 / 2.6

Notation: F_{fs}: free-surface fluctuation frequency; F_{toe}: jump toe oscillation frequency.

Free-surface deformation and wave celerity
Since some relationship was noted between the horizontal and vertical roller surface motions with comparable characteristic frequency ranges, the coupling between the motions was investigated and some simultaneous free-surface deformations in the two directions were documented. A cross-correlation analysis was performed between the longitudinal jump front position data and water elevation data. The results yielded some correlation functions as shown in Figure 8A. In Figure 8A, the cross-correlation functions were obtained between the horizontal displacement meter data and vertical displacement meter data at two different longitudinal positions of the same flow rate. In Figure 8A, a relative positive peak is seen for $(x-x_1)/d_1$ = 7.8, and a relative negative peak is shown for $(x-x_1)/d_1$ = 17.1 at about τ = 0 where τ is the time lag. Herein, the relative peak values were considered because an absolute correlation coefficient might be affected by some outside interference including electrical noise from the data acquisition system and long-term movements of jump roller. The relative positive maximum correlation coefficient indicated that the local free-surface elevation increased when the jump toe moved upstream and decreased when the jump toe moved downstream. Contrarily, the relative negative minimum correlation coefficient indicated the opposite trends. All the data showed close trends for all different flow conditions: that is, ΔR_{max} > 0 for $(x-x_1)/d_1$ < 11 and ΔR_{max} < 0 for $(x-x_1)/d_1$ > 11. The finding suggested two free-surface deformation trends at positions close to and far from the jump toe, as briefly sketched in Figure 8B (Black and red arrows).
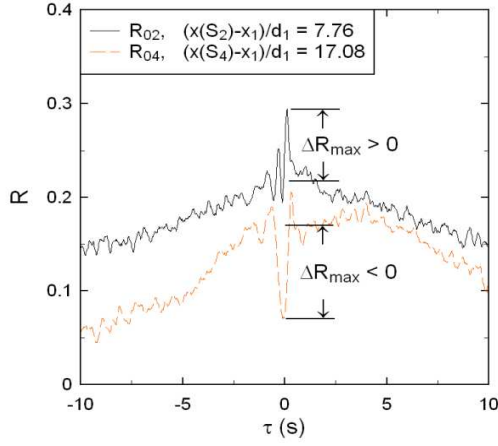
(A) Cross-correlation functions between horizontal and vertical free-surface motion data - Flow conditions: $Q = 0.0463$ m^3/s, $d_1 = 0.0322$ m, $x_1 = 1.25$ m, $Fr_1 = 5.1$, $Re = 9.2\times10^4$

$(x-x_1)/d_1 = 11$
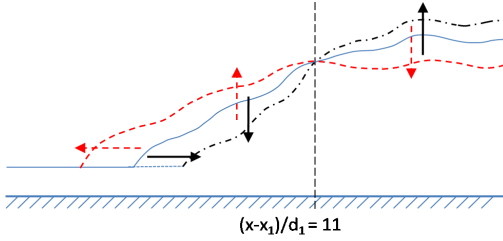
(B) Simultaneous horizontal and vertical roller surface motions (Black and red arrows)
Figure 8: Free-surface deformation analysis: (A, top) Experimental cross-correlation functions between horizontal and vertical free-surface motion data; (B, bottom) Simultaneous horizontal and vertical roller surface motions.

Visually the fluctuations in the roller surface tended to propagate downstream as turbulent flow structures formed and were advected in the roller. The wave celerity at the free-surface fluctuations U was derived based upon the signals of adjacent displacement meters above the roller, and compared with the advection velocity of large scale vortices in the roller V_{ej} (Fig. 2). Both U and V_{ej} are sketched in Figure 2. Herein U was calculated as $U = \Delta x/\Delta t$, where Δx is the longitudinal distance between the two displacement meters and Δt is the time lag for which the cross-cross-correlation function was maximum. The wave celerity was calculated along the channel centreline. The ratio of wave celerity to average inflow velocity U/V_1 is presented in Figure 9. The experimental results indicated basically a constant celerity of free-surface wave propagation independently of both the longitudinal location and Reynolds number, with an average value $U/V_1 = 0.39$. Figure 9 also includes the average advection velocities of large vortices in the roller V_{ej}/V_1 observed by Chanson (2010) and Zhang et al. (2013). The data were close, with mean values of 0.32 and 0.41 respectively (Fig. 9). Altogether the experimental data implied that the propagation of free-surface fluctuations above the roller was likely linked to the advection of large scale vortices in the shear layer.
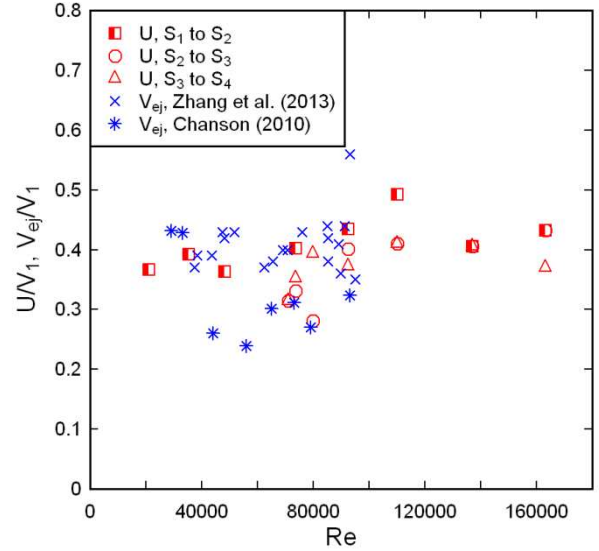

Figure 9: Ratio of wave celerity in the free-surface to average inflow velocity – Comparison with the average large vortices advection velocity data of Chanson (2010) and Zhang et al. (2013).

**Basic two-phase flow properties**
In the bubbly flow region, the phase-detection probe recorded the time series of local instantaneous void fraction c. The time-averaged void fraction C and bubble count rate F were derived from the raw signal. Figure 10 shows some typical vertical distributions of time-averaged void fraction and dimensionless bubble count rate for the same flow conditions at two different longitudinal positions. The data highlighted two air-water flow regions: that is, a shear layer between the channel bed and the elevation of a local minimum void fraction y^*, and a recirculation region between y^* and the roller free-surface. The shear layer was characterised by the advection of large vortices generated at the impingement point. In this region, the time-averaged void fraction and bubble count rate exhibited marked maxima, but at different elevations. The recirculation region was characterised by some air-water flow recirculation next to the free-surface together with spray and splashing above. The void fraction increased monotonically from the local minimum to unity, whereas the bubble count rate data indicated a secondary peak about C ~ 0.5.
The void fraction distribution followed a simplified theoretical solution in the shear layer (Chanson 1995,2010):

$$C = C_{max} \times exp\left[-\frac{1}{4 \times D^{\#}} \times \frac{\left(\frac{y - y_{C_{max}}}{d_1}\right)^2}{\left(\frac{X - X_1}{d_1}\right)}\right] \quad (6)$$

where C_{max} is the maximum time-averaged void fraction in the shear layer at an elevation $y = y_{Cmax}$ and $D^{\#}$ is the dimensionless diffusivity: $D^{\#} = D_t/(V_1\times d_1)$ with D_t being the air bubble diffusivity. Equation (6) is compared with the physical data in Figure 10. As illustrated in Figure 10, both the maximum of void fraction C_{max} and dimensionless bubble count rate $F_{max}\times d_1/V_1$ were found to decrease with increasing distance from the jump toe. The decay rates along the roller were mostly affected by the inflow Froude number for C_{max} and Reynolds number for $F_{max}\times d_1/V_1$. The corresponding elevations y_{Cmax} and y_{Fmax} increased linearly

with increasing longitudinal distances respectively.
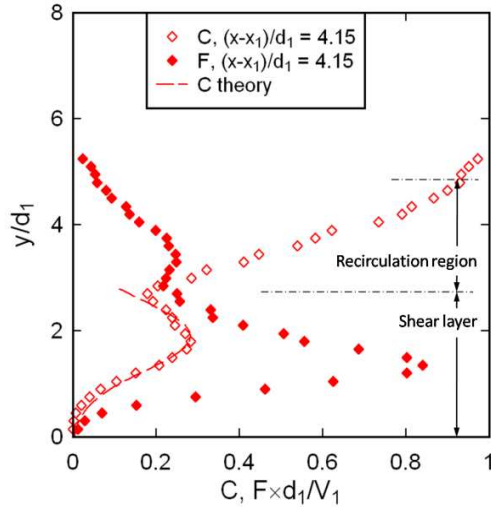
(A) $(x-x_1)/d_1 = 4.15$
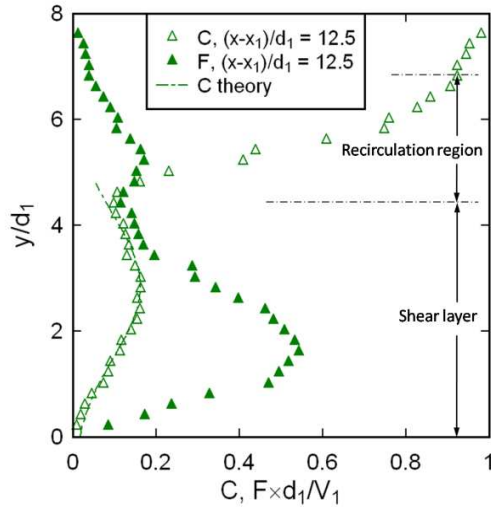
(B) $(x-x_1)/d_1 = 12.5$

Figure 10: Time-averaged void fraction and bubble count rate distributions in jump roller, sampled at 20 kHz for 45 s – flow conditions: $Q = 0.0333$ m^3/s, $d_1 = 0.020$ m, $x_1 = 0.83$ m, $Fr_1 = 7.5$, $Re = 6.6 \times 10^4$: (A, top) $(x-x_1)/d_1 = 4.15$; (B, bottom) $(x-x_1)/d_1 = 12.5$.

Simultaneous free-surface and air-water flow property fluctuations

The instantaneous void fraction c in the jump roller and the relative horizontal and vertical roller surface positions, η_x & η_y respectively, were measured simultaneously using the phase-detection probe and acoustic displacement meters (Fig. 3B). The signals were sampled synchronously at 5 kHz for 180 s and filtered to eliminate high-frequency component with a period less than the response time of the displacement meter (Murzyn & Chanson 2009a, Chachereau & Chanson 2011). The cross-correlation calculations were performed between the horizontal jump front position data η_x and instantaneous void fraction data c, and between the data of water elevation η_y and instantaneous void fraction. The correlation coefficients were denoted $R(\eta_x c)$ and $R(\eta_y c)$ respectively. Herein the measurements were performed with the same Froude number $Fr_1 = 5.1$ but various gate openings $h = 0.020, 0.030$ & 0.040 m, hence different Reynolds

numbers (Table 1). The void fraction measurements were performed at two cross-sections in the first half roller, with approximate longitudinal positions $(x-x_1)/d_1 = 4$ & 8.

The results showed some similar cross-correlation function profiles at the same elevations of phase-detection probe y/d_1 for different flow conditions. Two types of correlation function shapes were obtained, as illustrated in Figure 11. In Figure 11, a positive correlation function was calculated with the phase-detection probe in the lower shear layer ($y/d_1 = 0.7$). Positive peaks were seen at around $\tau = 0$ for both $R(\eta_x c)$ and $R(\eta_y c)$, indicating both increasing η_x and η_y when the instantaneous void fraction increased. That is, an upstream-moving jump toe and a rising free-surface elevation as more entrapped air was detected in the lower shear layer. When the void fraction was measured in the recirculation region ($y/d_1 = 2.6$), a negative correlation function was seen, with negative minimum correlation coefficient for $R(\eta_x c)$ with a negative time lag $\tau < 0$, and for $R(\eta_y c)$ at $\tau = 0$ (Fig. 11). The result implied that the instantaneous void fraction increased when the local water level dropped, followed by a downstream movement of the jump toe. The trends in terms of the simultaneous horizontal and vertical surface motions were consistent with the finding by coupling between the corresponding displacement meter signals, as shown in Figure 8 for $(x-x_1)/d_1 < 11$.
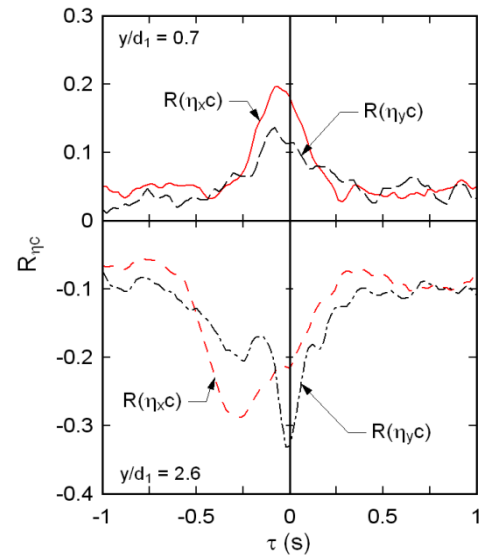

Figure 11: Typical cross-correlation functions between free-surface and instantaneous void fraction fluctuations.

The vertical distributions of maximum cross-correlation coefficients $R(\eta_x c)_{max}$ and $R(\eta_y c)_{max}$ are presented in Figure 12 together with the time-averaged void fraction C. Both $R(\eta_x c)_{max}$ and $R(\eta_y c)_{max}$ were positive in the lower shear layer, approximately $0 < y < y(C = 0.1)$, and negative in the recirculation region ($y > y^*$). In between, i.e. $y(C = 0.1) < y < y^*$, the maximum correlation coefficients had opposite signs: that is, $R(\eta_x c)_{max} < 0$ and $R(\eta_y c)_{max} > 0$. The occurrence of opposite signs implied that, in that region ($y(C = 0.1) < y < y^*$), the void fraction increased together with a downstream jump toe motion and increased free-surface elevation above the roller. The free-surface motions might reflect the flow bulking as well as some highly-aerated large-scale vortices detachment at the jump

toe. Direct correlation between the horizontal and vertical free-surface fluctuations did not reveal these instantaneous motions in a statistical sense, especially with the consideration of air entrainment processes. The interactions between horizontal and vertical free-surface fluctuations and air entrainment are sketched in Figure 13,. Figure 13 illustrates several void fraction measurement locations (note the different elevations of phase-detection probe) and the range of surface motion.
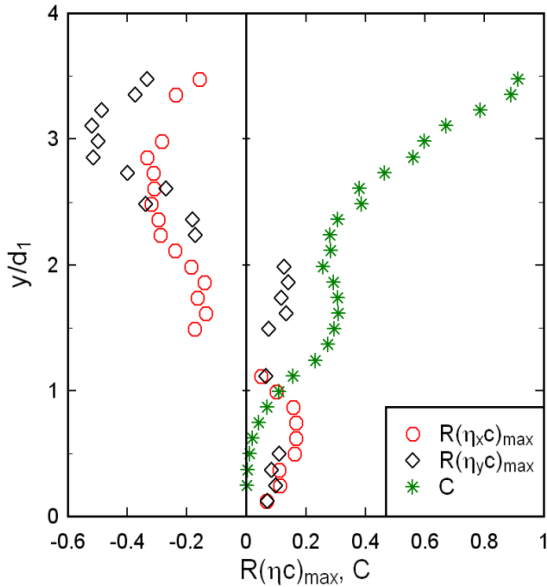

Figure 12: Distributions of maximum correlation coefficients between free-surface motions and instantaneous void fraction together with time-average void fraction – flow conditions: $Q = 0.0461$ m^3/s, $d_1 = 0.0322$ m, $x_1 = 1.25$ m, $x-x_1 = 0.125$ m, $Fr_1 = 5.1$, $Re = 9.2 \times 10^4$.
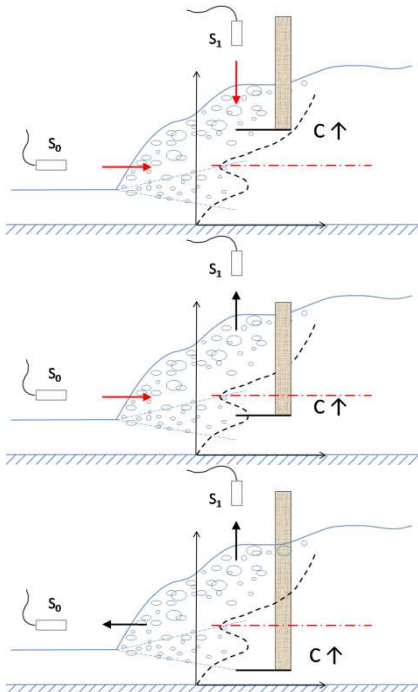

Figure 13: Sketches of free-surface deformations suggested by void fraction data in different region of roller: (A, top) void fraction in recirculation region; (B, middle) void fraction in middle shear layer; (C, bottom) void fraction in lower shear layer.

Conclusion

The free-surface fluctuations and air-water flow properties of turbulent hydraulic jumps were investigated physically using some non-intrusive acoustic displacement meters and intrusive phase-detection probe. The measurements were performed mostly on the channel centreline, for a range of Froude numbers ($3.8 < Fr_1 < 10.0$) for a constant upstream water depth, and for a range of Reynolds numbers ($2.1 \times 10^4 < Re < 1.6 \times 10^5$) for a given Froude number.

The time-averaged free-surface profile was well defined, presenting some self-similarity along the length of roller. The largest free-surface fluctuations were observed in the first half roller, and the maximum fluctuations increased with increasing inflow Froude number. Some frequency analyses were performed in terms of both vertical and horizontal free-surface fluctuations. The results highlighted some dominant and secondary characteristic frequencies for both motions. A cross-correlation analysis showed that the horizontal and vertical motions interacted, the coupling being reflected by the secondary frequencies. The Froude number was a dominant factor in terms of the dimensionless free-surface vertical fluctuation frequencies, while some effects of the Reynolds number were shown onto the horizontal jump toe oscillations. A cross-correlation analysis of the simultaneous horizontal and vertical fluctuating motions showed different types of free-surface deformation before and after the position $(x-x_1)/d_1 = 11$. The wave celerity at the roller free-surface was about $0.4 \times V_1$, close to the observed advection velocity of large vortices in the shear layer. The present non-intrusive measurement results showed some agreement with previous studies, although the study herein covered a wider range of measured parameters and flow conditions.

Basic air-water flow properties were measured including void fraction and bubble count rate. Maximum values were observed in the shear layer, but at different elevations. Both the maximum void fraction and maximum bubble count rate exhibited some longitudinal decay with increasing distance from the jump toe. The decay rate of maximum void fraction and maximum dimensionless bubble count rate were affected mostly by the Froude and Reynolds numbers respectively. Simultaneous measurements of vertical and horizontal free-surface fluctuations and instantaneous void fraction highlighted the coupling between the free-surface fluctuations and air-water flow properties. The results suggested that, at longitudinal positions close to the jump toe, the air entrapment increased in the lower shear layer when the roller moved upstream, whereas it decreased in the recirculation region. Between the lower shear layer and recirculation region, the jump toe tended to move downstream when more entrapped air was detected, together with some flow bulking of the roller surface.

Acknowledgements

References

Chachereau, Y. & Chanson, H. Free-Surface Fluctuations and Turbulence in Hydraulic Jumps. Experimental Thermal and Fluid Science, Vol. 35, No. 6, 896-909 (2011).

Chanson, H. Air Entrainment in Two-Dimensional Turbulent Shear Flows with Partially Developed Inflow Conditions. Journal of Multiphase Flow, Vol. 21, No. 6, 1107-1121 (1995).

Chanson, H. Air Bubble Entrainment in Hydraulic Jumps: Similitude and Scale Effects. Report No. CH57/05, Dept. of Civil Engineering, the University of Queensland, Brisbane, Australia (2005).

Chanson, H. Dynamic Similarity and Scale Effects Affecting Air Bubble Entrainment in Hydraulic Jumps. Proceedings of 6th International Conference on Multiphase Flow ICMF 2007, Leipzig, Germany, July 9-13 (2007).

Chanson, H. Turbulent Air-water Flows in Hydraulic Structures: Dynamic Similarity and Scale Effects. Environmental Fluid Mechanics, Vol. 9, No. 2, pp. 125-142 (DOI: 10.1007/s10652-008-9078-3) (2009).

Chanson, H. Convective Transport of Air Bubbles in Strong Hydraulic Jumps. International Journal of Multiphase Flow, Vol. 36, No. 10, 798-814 (2010).

Chanson, H. Hydraulic Jumps: Turbulence and Air Bubble Entrainment. La Houille Blanche, Vol. 3, 5-16 (2011).

Liggett, J.A. Fluid Mechanics. McGraw-Hill, New York, USA (1994).

Kucukali, S. & Chanson, H. Turbulence Measurements in Hydraulic Jumps with Partially-Developed Inflow Conditions." Experimental Thermal and Fluid Science, Vol. 33, No. 1, pp. 41-53 (DOI: 10.1016/j.expthermflusci.2008.06.012) (2008).

Leandro, J., Carvalho, R., Chachereau, Y. & Chanson, H. Estimating Void Fraction in a Hydraulic Jump by Measurements of Pixel Intensity. Experiments in Fluids, Vol. 52, No. 5, pp. 1307-1318 (DOI: 10.1007/s00348-011-1257-1) (2012).

Long, D., Rajaratnam, N., Steffler, P.M. & Smy, P.R. Structure of flow in hydraulic jumps. Journal of Hydraulic Research, IAHR, Vol. 29 (2), pp. 207–218 (1991).

Madsen, P.A. A Model for a Turbulent Bore, Ph.D. Thesis, Technical University of Denmark, Institute of Hydrodynamics and Hydraulic Engineering, Copenhagen, Denmark, 149 pages (1981) (also Series Paper No. 28, Technical University of Denmark, Institute of Hydrodynamics and Hydraulic Engineering, Copenhagen, Denmark, 149 pages (1981)).

Mossa, M. & Tolve, U. Flow visualization in bubbly two phase hydraulic jumps, Journal of Fluids Engineering, Transactions of the ASME, Vol. 120, 160–165 (1998).

Mouaze, D., Murzyn, F. & Chaplin, J.R. Free Surface Length Scale Estimation in Hydraulic Jumps. Jl of Fluids Eng., Trans. ASME, Vol. 127, pp. 1191-1193 (2005).

Murzyn, F. & Chanson, H. Free-Surface Fluctuations in Hydraulic Jumps: Experimental Observations. Experimental Thermal and Fluid Science, Vol. 33, No. 7, pp. 1055-1064 (DOI: 10.1016/j.expthermflusci.2009.06.003) (2009a)

Murzyn, F. & Chanson, H. Experimental Investigation of Bubbly Flow and Turbulence in Hydraulic Jumps. Environmental Fluid Mechanics, Vol. 9, No. 2, 143-159 (2009b).

Zhang, G.F., Wang, H. & Chanson, H. Turbulence and Aeration in Hydraulic Jumps: Free-Surface Fluctuation and Integral Turbulent Scale Measurements. Environmental Fluid Mechanics, Vol. 13 (DOI 10.1007/s10652-012-9254-3) (2013). (In print)